

UNIVERSIDAD DE LOS ANDES



Phenomenological Study of Search of Heavy Neutrinos, with Displaced Vertices and Vector Boson Fusion

THIS DISSERTATION IS SUBMITTED FOR THE DEGREE OF

PHYSICIST

BY

SANDRA JIMENA GONZÁLEZ LOZANO

ADVISOR: ANDRÉS FLÓREZ

BOGOTÁ, D.C.

2017

Contents

1	Introduction	1
2	State of the Art	5
2.1	Standard Model	5
2.2	Neutrinos in the Standard Model	7
2.2.1	Dirac Mass	7
2.2.2	Majorana Mass	8
2.3	Seesaw Mechanism	10
3	Important Concepts	13
3.1	Jets	13
3.2	Cross Section and Luminosity	14
3.3	Pseudorapidity	15
3.4	p_T , $E_T^{\vec{miss}}$ and H_T	16
3.5	Displaced Vertices and Impact Parameter	17
4	CMS Detector	19
4.1	Tracking System	20
4.2	Calorimetry	22
4.2.1	Electromagnetic Calorimeter	22
4.2.2	Hadron Calorimeter	23
4.3	Muon Detector	23
4.4	Triggers	25
5	Modeling of signal and backgrounds	27
5.1	Signal of Interest	27

5.2	Backgrounds	29
5.2.1	W+Jets Background	30
5.2.2	Drell Yan + Jets Background	30
5.2.3	$t\bar{t}$ Background	31
6	Methodology	33
6.1	MadGraph	33
6.2	Pythia	34
6.3	Delphes	35
6.4	ROOT	35
7	Event Selection Criteria	37
8	Analysis	41
9	Conclusions	51
Appendix A	Neutrinos and Seesaw Mechanism	53
A.0.1	Dirac Mass	53
A.0.2	Majorana Mass	54
A.0.3	Seesaw Mechanism	56

List of Figures

2.1	Particles of the Standard Model	6
3.1	Description of a jet at three different levels: partonic, hadronic and detector. Image taken from [15]	14
3.2	CMS and ATLAS detector coordinates. Image taken from [18]	15
3.3	Scheme of a displaced vertex. Image taken from [19]	17
3.4	Scheme of the impact parameter variable. Image taken from [20]	18
4.1	CMS detector. Image take from [21]	20
5.1	Signal Feynman diagrams	29
5.2	Feynman diagram for the W+jets Background	30
5.3	Feynman diagram for the DY+jets Background	31
5.4	Feynman diagram for $t\bar{t}$ Background	32
8.1	Stacked plot of E_T^{miss} after the preselection cuts and cuts on the number of jets, taus and b-jets.	42
8.2	Stacked plot of H_T after the preselection cuts and cuts on the number of jets, taus and b-jets.	43
8.3	Stacked plot of di-jet mass after the preselection cuts and cuts on the number of jets, taus and b-jets.	44
8.4	Stacked plot of $p_T(\tau)$ after the preselection cuts and cuts on the number of jets, taus and b-jets.	45
8.5	Stacked plot of H_T after the all the cuts were imposed. . . .	46
8.6	Stacked plot of di-jet mass after the all the cuts were imposed.	47

8.7	Stacked plot of $p_T(\tau)$ after the all the cuts were imposed. . .	48
8.8	2D plot: E_T^{miss} vs d_{xy}	49
8.9	2D plot: $p_T(\tau)$ vs $ d_{xy} $	49

Chapter 1

Introduction

The Standard Model (SM) is a theory that collects our knowledge about the elementary particles and their interactions. Despite this theory is capable of explaining several physical phenomena that have been observed in experiments, there are some questions that this model does not answer. Thus, this theory is not complete. For example, several cosmological observations suggest the existence a new type of matter that is stable and that does not interact electromagnetically, referred to as dark matter (DM). Unfortunately, the SM does not provide a particle that fulfills the required characteristics of DM. Other dilemma the SM has is related to the mass of neutrinos: it predicts that the neutrino mass is zero. Nevertheless, the former is incorrect because the observation of neutrinos oscillations in multiple experiments demonstrates that neutrinos have mass [1, 2]. One additional fact that is very interesting and the SM can not explain is the observation of neutrinos with only left-handed helicity.

This monograph focuses in models that propose the existence of heavy-neutrinos with right-handed helicity, which in some cases are postulated as DM candidates [3, 4]. Additionally, these models propose a mechanism by which neutrinos acquire mass. The Seesaw mechanism is a popular extension of the SM that includes heavy right-handed neutrinos. If the existence of these particles is proved, not only the helicity symmetry of neutrinos would be restored, but also it would explain how they gain mass. The search of these particles has been performed in the experiments LEP [5], CMS [6] and ATLAS [7] without successful results yet.

Recently, it has been proposed a new mechanism of production of heavy neutrinos through the decay of the Higgs Boson [8] using the Type I Seesaw mechanism. If the heavy neutrino mass is of the order of a few GeV, the Higgs boson would travel a certain distance before decaying. As a consequence, the decay products are expected to have associated tracks with displaced vertices. In this case the presence of tracks with displaced vertices in the detector is an important signal to prove the Seesaw mechanism. Nevertheless, due to experimental restrictions of the available triggers in CMS and ATLAS, the theoretical analysis proposed in reference [8] is not achievable. This project proposes the production mechanism of the Higgs boson through Vector Boson Fusion (VBF), instead of gluon annihilation (Drell-Yan). The VBF jets in the event topology gives a new handle in order to trigger on these hypothetical signal events.

The observation of the Higgs decay into heavy neutrinos would be a firm proof of the Type I Seesaw mechanism [9], which would indicate the existence of physics beyond the SM. The Type I Seesaw mechanism is the simplest extension of the SM that is capable of explaining the smallness of the left-handed neutrino masses with respect to other fundamental particles.

The main problem of detecting this event of interest is that the magnitude of its signal is significantly small with respect to other processes from the SM. For this reason, the processes from the SM that have the same or similar final states as the signal of interest are called backgrounds. Therefore, it is fundamental to develop procedures with the objective of reducing the experimental backgrounds under the magnitude of the searched signal. These procedures use different variables that exploit the topology of the event and its kinematic characteristics. When a set of variables that potentially separate the signal from the background are determined, it is necessary to find the optimal values of these variables that allow to reduce as much as possible the background. Generally, the optimization studies use figures of significance, such as:

$$\frac{S}{\sqrt{S+B}}, \quad (1.1)$$

where S and B represent the expect number of signal and background events respectively.

This document is organized as follows. In Chapter 2 the state of the art for this study is stated: the SM is described and the Seesaw mechanism is explained. Then, in Chapter 3 the important concepts for this analysis, such as jets, luminosity, cross section, etc, are described. Additionally, the kinematical variables used in this analysis that have the potential of reducing the levels of background are defined and illustrated in this chapter. The simulation of the interaction of particles with a detector, was performed using the emulation of the CMS detector. The description of the CMS detector is found in Chapter 4. In this chapter there is also a brief description of the triggers performed at the CMS. In Chapter 5 there is an explanation of the topology of the signal and its possible final states. In Chapter 6 there is a description of the software tools used in this analysis. The computational programs used were: MadGraph which makes a simulation of the event, Pythia which simulates the processes of hadronization of the signal, Delphes which simulates the behaviour of a multipurpose detector, and ROOT that is used to perform the analysis of the signal and backgrounds. The pre-selection criteria and required cuts used in the study, with the corresponding motivation, are explained in Chapter 7. In Chapter 8, the analysis technique used for this study is described, and it is showed the performance of different variables and their potential to reduce the background is discussed. Finally, in Chapter 9 the conclusions of this project are stated.

Chapter 2

State of the Art

2.1 Standard Model

The SM is a theory that explains how the fundamental blocks of the universe interact through the fundamental forces of nature. This model is based on a quantum field theory which incorporates relativity and quantum mechanics. The SM also classifies the fundamental particles and the compound ones.

According to this model there are two types of fundamental particles in nature: bosons and fermions. Fermions are the particles that make up matter, while bosons transmit interactions through their exchange. Bosons have integer spin while fermions have half-integer spin. There are two classifications of fermions: quarks and leptons. Quarks have a characteristic property called color charge. There are three types of color charge referred to as: blue, red and green. A distinctive characteristic of quarks and their color interaction is "color confinement", which prevents quarks from being isolated singularly (free). Because of this property, quarks are only found grouped as hadrons. Thus, hadrons are defined as composite subatomic particles and there are two types: baryons and mesons. Baryons are conformed by three quarks (anti-quarks) and mesons by quark-anti-quark pairs. The other type of fermions are leptons, which do not have color charge.

The SM explains three fundamental interactions: electromagnetic, strong and weak, but it does not include the gravitational interaction. The elec-

tromagnetic interaction acts on particles that have electric charge, it is transmitted by photons, and it has an infinite range. The strong interaction affects color charged particles and it is mediated by gluons, which carry color charge. The range of strong interaction is just around 10^{-15} m (the order of the diameter of a medium sized nucleus). The weak interaction appears in the radioactive decay, which is the process responsible of the decay of unstable nuclei. The radioactive decay is caused when there is a greater quantity of protons than neutrons. The weak force is transmitted through three bosons W^\pm and Z^0 . Since the mass of each of these particles is relatively large, the weak interaction has a short range of around 10^{-18} m.

Figure 2.1: Particles of the Standard Model

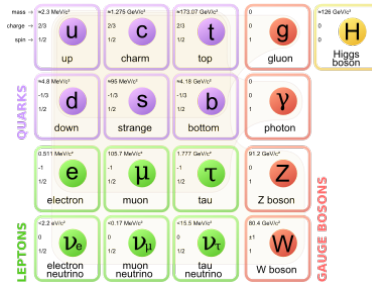


Figure 2.1 shows the particles of the SM and specifies their properties. Fermions are grouped into three generations, each having two quarks and two leptons. Each member of a higher generation has a greater mass than the corresponding particle of the previous generation. Each generation contains one quark with charge $-1/3e$ (down-type) and other with charge $+2/3e$ (up-type). For leptons, each generation includes one with $-e$ charge lepton and one neutral lepton (called neutrino) related to the corresponding lepton. Their classification is: first generation contains electron and electron neutrino, the second generation includes muon and muon neutrino, and third generation includes tau and tau neutrino. The SM also postulates that for each known particle there exists another particle with the same value of mass and spin, opposite electric charge, and different color charge. This partner is called antiparticle.

Additionally, according to the SM, the fundamental particles acquire

their mass through their interaction with a scalar field denominated Higgs field. The mediating particle of this field is the Higgs boson and it was discovered in 2012 as announced by the experiments CMS and ATLAS [10, 11].

As it was mentioned earlier, although the SM explains different phenomena, it is not a complete theory since there are physical observations that this theory does not explain. For example, as it was mentioned earlier, it predicts that neutrinos have zero mass but observations neutrino oscillations indicate the opposite. Moreover, the SM does not provide a possible candidate for DM and does not explain the asymmetry of the neutrinos helicity. For this reason, some theories that extend the reach of SM have been proposed. The simplest extension of SM that can explain the smallness of neutrino masses is Type I Seesaw mechanism.

2.2 Neutrinos in the Standard Model

As it was mentioned earlier, the SM does not explain the reason why the mass of neutrinos is a factor of almost 10^{-6} smaller than the mass of the other fermions. Moreover, the SM predicts that the mass of the neutrinos is zero. Additionally, it does not provide an explanation to the fact that only left-handed neutrinos have been observed in nature. In this section some of the possible solutions to these problems are stated.¹

2.2.1 Dirac Mass

First, we start by studying the Dirac mass term of a free fermion. The Lagrangian equation for a fermion particle is given by the expression:

$$L = \bar{\psi}(i\gamma^\mu\partial_\mu - m)\psi, \quad (2.1)$$

where ψ is the Dirac Spinor. From this Lagrangian expression, it is possible to see that in the SM the mass is included through the second term in the equation which is called “Dirac mass term”:

$$m\bar{\psi}\psi \quad (2.2)$$

¹The detailed calculations of the theory explained here are stated in A

We can write the Dirac Spinor as a sum of its left- and right- chiral states:

$$m\bar{\psi}\psi = m(\bar{\psi}_L + \bar{\psi}_R)(\psi_L + \psi_R) = m\bar{\psi}_L\psi_R + m\bar{\psi}_R\psi_L \quad (2.3)$$

In the last expression we used the fact that: $\bar{\psi}_L\psi_L = \bar{\psi}_R\psi_R = 0$ which is proved in Appendix A. It can be seen from Equation 2.3 that a massive particle must have both quiral states: left and right. Thus, the Dirac mass can be interpreted as the coupling constant between the two chiral states. Since right-handed neutrinos have never been observed in nature, it is expected that neutrinos have zero mass. Nevertheless, experiments of neutrino oscillations indicate that neutrinos have a small mass of the order of MeV. This implies either the existence of a right-handed neutrino which will explain the small mass of the left-handed neutrinos, or that there exists other sort of mass term [12].

2.2.2 Majorana Mass

The Majorana Mechanism is based on expressing the mass term in the Lagrangian in only the left-handed chiral state terms. To do this we start by decomposing the wavefunction into its left and right chiral states in the Dirac Lagrangian [13]:

$$\begin{aligned} L &= \bar{\psi}(i\gamma^\mu\partial_\mu - m)\psi \\ &= (\bar{\psi}_L + \bar{\psi}_R)(i\gamma^\mu\partial_\mu - m)(\psi_L + \psi_R) \\ &= i\bar{\psi}_L\gamma^\mu\partial_\mu\psi_L - \bar{\psi}_L m\psi_R + i\bar{\psi}_R\gamma^\mu\partial_\mu\psi_R - \bar{\psi}_R m\psi_L \end{aligned} \quad (2.4)$$

In the Equation 2.4, we used $\bar{\psi}_L\psi_L = \bar{\psi}_R\psi_R = 0$ and $\bar{\psi}_R\gamma^\mu\partial_\mu\psi_L = \bar{\psi}_L\gamma^\mu\partial_\mu\psi_R = 0$. These expressions are explained in the Appendix A. Now, we can replace the expression of this Lagrangian in the Euler-Lagrange equation:

$$\frac{\partial L}{\partial(\partial\phi)} - \frac{\partial L}{\partial\phi} = 0 \quad (2.5)$$

By doing this, we find that the two equations of motion for the fields are two coupled Dirac equations for the right- and left- handed fields:

$$i\gamma^\mu \partial_\mu \psi_L = m\psi_R \quad (2.6)$$

$$i\gamma^\mu \partial_\mu \psi_R = m\psi_L \quad (2.7)$$

In the formulation of the SM, the mass of the neutrino is zero. In this case, we obtain two equations which are called “Weyl equations”:

$$i\gamma^\mu \partial_\mu \psi_L = 0 \quad (2.8)$$

$$i\gamma^\mu \partial_\mu \psi_R = 0 \quad (2.9)$$

The former means that neutrinos can be described using two two-component spinors that are helicity eigenstates. These eigenstates represent two states with definite and opposite helicity which correspond to the left- and right-handed neutrinos. However, since we have not observed a right-handed neutrino we just represent the neutrino as a single left-handed massless field [12].

Majorana discovered a way to describe a massive neutrino just in terms of its left-handed field. This calculation is performed in the Appendix A. The objective of Majorana was to write the Equation 2.7 as 2.6 by finding an expression for ψ_R in terms of ψ_L . By doing some manipulations of the Equation 2.7 we find that it can be written as:

$$i\gamma^\mu \partial_\mu C\bar{\psi}_R^\top = mC\bar{\psi}_L^\top, \quad (2.10)$$

where C is the operator charge conjugation operator. Now, Equation 2.10 would have the same structure as Equation 2.6 if the right-handed term is imposed to be:

$$\psi_R = C\bar{\psi}_L^\top \quad (2.11)$$

The former assumption requires $C\bar{\psi}_L^\top$ to be right-handed, which is proved in the Appendix A. Thus, the complete Majorana field can be written as:

$$\psi = \psi_L + \psi_R = \psi_L + C\bar{\psi}_L^\top \quad (2.12)$$

Defining the charge-conjugate field as: $\psi_L^C = C\bar{\psi}_L^\top$, the Majorana field can be expressed as:

$$\psi = \psi_L + \psi_L^C \quad (2.13)$$

The implications of requiring the right-handed component of ψ to satisfy the Equation 2.13 can be studied by taking the charge conjugate of the complete Majorana field.

$$\psi^C = (\psi_L + \psi_L^C)^C = \psi_L^C + \psi_L = \psi \quad (2.14)$$

Having in mind that the charge conjugation operator turns a particle state into an antiparticle state, it can be deduced that a Majorana particle is its own antiparticle. Since the charge conjugation operator flips the sign of electric charge, a Majorana particle must be neutral. Thus, the neutrino is the only fermion that could be a Majorana particle.

Majorana Mass Term

In Equation 2.3 we saw that the mass term in the Lagrangian couples the left and right chiral states of the neutrino. Replacing the expression we found in Equation 2.11 for the right-handed component of the neutrino field in the mass term of the Lagrangian, we get equation 2.15 [13]. In this equation ν represents the neutrino.. Having in mind that the hermitian conjugated of the first term in the equation is identical, we normalize the Lagrangian and obtain:

$$L_{Maj}^L = m\overline{\nu_L}\nu_L^C + m\overline{\nu_L^C}\nu_L = \frac{1}{2}m\overline{\nu_L^C}\nu_L \quad (2.15)$$

2.3 Seesaw Mechanism

As it was mentioned before, in the case that the right-handed chiral field does not exist, there can be no Dirac mass term. However, we can have a Majorana mass term in the Lagrangian (associated to a left-handed chiral field) so the neutrino would be a Majorana particle:

$$L_{Maj}^L = \frac{1}{2}m_L\overline{\nu^C}_L\nu_L \quad (2.16)$$

In order to let the neutrino have mass, a right-handed neutrino that interacts gravitationally must exist. If we consider that a right-handed

chiral neutrino can exist, we would have to add different terms to the Lagrangian. First, if we assume that it is possible to write a left-handed Majorana field, we have for the first term:

$$L_L^M = m_L \bar{\nu}_L \nu_L^C + m_L \bar{\nu}_L^C \nu_L \quad (2.17)$$

Additionally, we have to include a similar term which is the right-handed Majorana field:

$$L_R^M = m_R \bar{\nu}_R^C \nu_R + m_R \bar{\nu}_R \nu_R^C \quad (2.18)$$

We also have to add Dirac mass terms in order to study the most general Lagrangian: the first Dirac mass term we mentioned on this section in Equation 2.19 and the term that comes from the charge-conjugate fields (Equation 2.20) [12]:

$$L = m_D \bar{\nu}_L \nu_R + m_D \bar{\nu}_R \nu_L \quad (2.19)$$

$$L = m_D \bar{\nu}_R^C \nu_L^C + m_D \bar{\nu}_L^C \nu_R^C \quad (2.20)$$

Since the hermitian conjugate of each equation is identical, we can write the most general mass term as a sum of the Lagrangians:

$$L = \frac{1}{2} \left(m_L \bar{\nu}_L^C \nu_L + m_R \bar{\nu}_R^C \nu_R + m_D \bar{\nu}_R \nu_L + m_D \bar{\nu}_L^C \nu_R^C \right) \quad (2.21)$$

The former equation can be written as a matrix equation:

$$L_{mass} \propto \begin{pmatrix} \bar{\nu}_L^C & \bar{\nu}_R \end{pmatrix} \begin{pmatrix} m_L & m_D \\ m_D & m_R \end{pmatrix} \begin{pmatrix} \nu_L \\ \nu_R^C \end{pmatrix} \quad (2.22)$$

Equation 2.22 expresses the Lagrangian in terms of the left and right chiral states. These states do not have a definite mass because the matrix is not diagonal. Thus, the left and right chiral states do not correspond to the physical particles (which have a definite mass). Instead, the real particles are the eigenstates of the matrix. In order to find the mass eigenvalues we need to diagonalize the mass matrix in Equation 2.22, referred to now as M . This calculation is explained in Appendix A. We find that the mass eigenstates are given by the expression:

$$m_{1,2} = \frac{1}{2} \left[(m_L + m_R) \pm \sqrt{(m_L - m_R)^2 + 4m_D^2} \right] \quad (2.23)$$

The fact that the SM does not allow a Majorana left-chiral mass term implies $m_L = 0$. Next, we are going to study the expression of the mass eigenstates m_1 and m_2 . When we choose $m_R \gg m_D$, we get for the mass eigenvalues:

$$m_1 = \frac{m_D^2}{m_R} \quad (2.24)$$

$$m_2 = m_R \left(1 + \frac{m_D^2}{m_R^2} \right) \approx m_R \quad (2.25)$$

From both equations above we can deduce that if a neutrino with mass m_2 very large exists, the other neutrino must have a small mass. This is the reason why this mechanism is called “Seesaw”: the mass of each physical neutrino is controlled by the mass eigenvalues in a way such that when one neutrino is light the other one is heavy [13]. Now, the neutrino mass eigenstates are given by the following expressions:

$$\nu_1 \propto (\nu_L + \nu_L^C) - \frac{m_D}{m_R^2} (\nu_R + \nu_R^C) \quad (2.26)$$

$$\nu_2 \propto (\nu_R + \nu_R^C) + \frac{m_D}{m_R^2} (\nu_L + \nu_L^C) \quad (2.27)$$

The Equations 2.26 and 2.27 show that ν_1 is mostly the left-handed light Majorana neutrino, while ν_2 is the heavy sterile right-handed neutrino. This is the explanation that the Seesaw Mechanism gives to the fact that the neutrino is much lighter than the other fermions. The described model in this section is the Type I Seesaw mechanism, and it the simplest extension to the SM that explains the smallness of the observed neutrino masses.

Chapter 3

Important Concepts

3.1 Jets

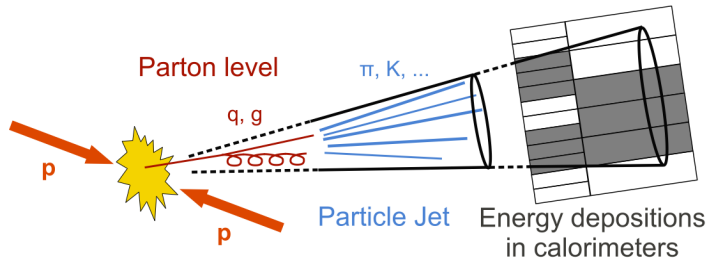
A jet can be defined as a high energy shower of stable particles that comes from fragmentation of quarks or gluons [14]. The initial quarks and gluons in the process are known as “initial partons”. Because partons have color charge,, they can not be isolated singularly. Since it is not possible for coloured particles to be isolated, they must go through a non-perturbative process that converts them into colour neutral particles. This process is called “hadronization”, and there are different models to explain it. According to the string model, the potential energy associated with the color charge increases proportionally with the distance between the partons. When the distance reaches a certain critical value, it is energetically favourable to produce a quark-anti-quark pair from the vacuum. Finally, by this process the initial colour charged particles are converted into bound colour-singlet hadronic states.

Despite jets may display a structure with properties that could indicate which were the initial partons interacting, they are hard to study individually when there is a numerous quantity of them in an event. The former is because it is almost imposible to associate all particles in an event final state to a single initial parton. The reconstruction of jets depends on elements like the fragmentation process, detectors effects, among others. Dedicated jet-reconstruction algorithms are used in order to determine the kinematic information of jets. The objective of these algorithms is to de-

termine the initial interacting partons and approximate its directions and energies.

According to the reconstruction algorithms, we can define a jet at three different levels. At parton level, a jet can be understood as a quark or a gluon. At hadronic level, can be referred to as the hadrons produced due to the partons fragmentation processes. Finally, at a detector level, a jet can be understood as a set of reconstructed tracks spatially associated with large energy depositions in the calorimeters [16]. The reconstruction algorithms that are going to be used for this analysis consist in the use of mathematical cones that enclose the regions where a large quantity of particles are detected. The radius of the cone must be large enough to enclose all the particles coming from the initial quark or gluon, and must be small enough to not include other particles that belong to a different jet. The three level definitions just mentioned are illustrated in Figure 3.1. In this figure the mathematical cones used for the reconstruction of a jet are also showed.

Figure 3.1: Description of a jet at three different levels: partonic, hadronic and detector. Image taken from [15]



3.2 Cross Section and Luminosity

In High Energy Physics, the cross section σ represents the probability that a given physical process occurs. This quantity is proportional to the energy of the colliding particles. The unit used for cross sections is the barn ($1b = 10^{-28}\text{m}^2$). The number of expected events of a certain interaction in a fixed target experiment is proportional to its cross section, the particle flux,

and the number of atoms per cubic meter in the target multiplied by the length [17]. The inverse of the number of atoms per area is called “target constant (F)” and it has the dimension of an area. Thus, it is possible to make an estimation of the number of interactions per second using:

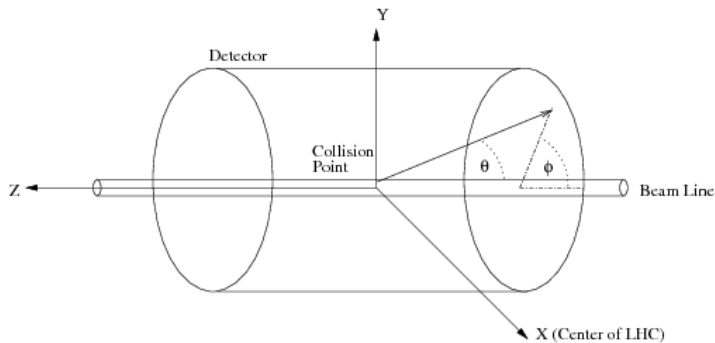
$$\frac{N_{events}}{s} = \sigma \times \frac{N_{flux}/s}{F} = \sigma \times Luminosity \quad (3.1)$$

In Equation 3.1, we defined the concept of luminosity, which depends on the beam energy and dynamics. The luminosity is a quantity that is used to describe the performance of a particle accelerator. It has units of the inverse of cross section, which is known as inverse barns fb^{-1} and it is equivalent to ($1fb = 10^{-28}m^2$).

3.3 Pseudorapidity

Pseudorapidity is a variable that is defined in terms of the polar angle. Figure 3.2 shows the coordinate system used by the ATLAS and CMS experiments at the LHC.

Figure 3.2: CMS and ATLAS detector coordinates. Image taken from [18]



The origin of the CMS and ATLAS coordinate system coincides with the point in which a collision occurs in the detectors. The polar angle is described by the parameter θ and it is measured with respect to the z axis. The azimuthal angle is denoted by Φ and it is measured in the xy plane

from the x axis. The pseudorapidity is defined in terms of the polar angle as:

$$\eta \equiv -\ln(\tan(\theta/2)) \quad (3.2)$$

The motivation to define and use this variable is that while $\Delta\theta$ is not a Lorentz invariant $\Delta\eta$ is. Furthermore, the quantity of particles depending on the variable η is approximately uniform in a cylindrical detector.

3.4 p_T , $E_T^{\vec{miss}}$ and H_T

The quantity p_T represents the transverse momentum, which is defined as the projection of the linear momentum onto the xy plane. This variable is used instead of the linear momentum because the initial beams are moving just in the z axis (the initial momentum in the xy plane is zero), so when a collision is produced the interesting effects occur in the transverse plane.

As it was already mentioned, the momentum in the transverse plane is zero before the collision. Since the transverse momentum has to be conserved, after the collision it must also be zero. We can write the total momentum as the sum of the particles that are detected (visible particles) and the ones that are not detected (invisible particles), which can be expressed as:

$$0 = \sum_{i=1}^N P_T^{\vec{i}} = \sum_{j=1}^M P_T^{\vec{j}}{}^{visible} + \sum_{k=M}^{N-M} P_T^{\vec{k}}{}^{invisible} \quad (3.3)$$

The Equation 3.3 motivates the definition of a variable called “missing transverse energy” ($E_T^{\vec{miss}}$), which is defined as the sum of the transverse momentum of the invisible particles:

$$E_T^{\vec{miss}} \equiv \sum_{k=M}^{N-M} P_T^{\vec{k}}{}^{invisible} = - \sum_{j=1}^M P_T^{\vec{j}}{}^{visible} \quad (3.4)$$

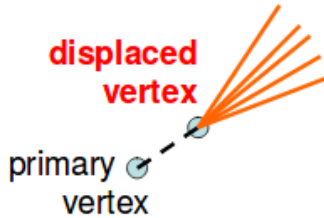
Finally, the variable H_T is defined as the scalar sum of the transverse momentum of all the jets in the event, as it is showed in Equation

$$H_T = \sum_i^n P_T(jet_i) \quad (3.5)$$

3.5 Displaced Vertices and Impact Parameter

The vertex of a track is a variable of importance because it can be used to determine the position of the point of interaction and the momentum vector of the tracks emerging from the vertex. The vertex recognition can also be used to check the association of tracks to a vertex, in other words, to determine if a track actually originates from a certain vertex. In order to determine the direction of the track connecting a primary and a secondary vertex, we have to find the position of the secondary vertex. Some particles can pass through the detector without leaving tracks. However, when these undetected particles decay, the particles produced can be observed because they leave tracks on the detector. The point at which the product particles are detected is called a secondary vertex, and it is said that it is a displaced vertex. Figure 3.3 shows a sketch of a displaced vertex, where the path of the undetected particle is represented by a dotted line.

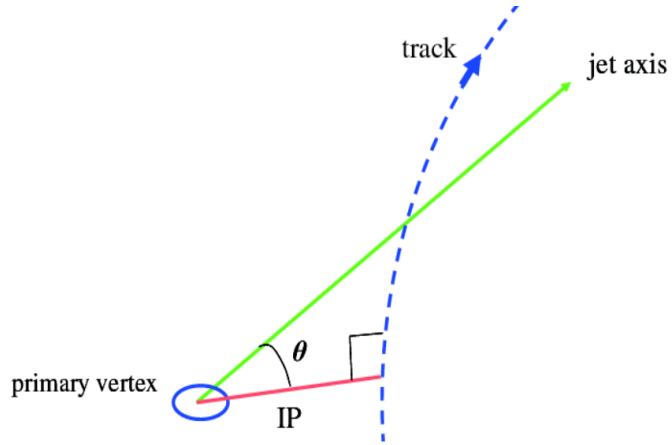
Figure 3.3: Scheme of a displaced vertex. Image taken from [19]



The impact parameter is defined as the closest distance between the vertex and the points of the track. A visualization of this is showed in Figure 3.4. In this image, the track is represented by the blue dotted line, and the impact parameter by the red line. It can be seen that the impact parameter line forms a right angle with the track. Using this characteristic it is possible to identify in a unique way the closest point of approach of

the track to the vertex.

Figure 3.4: Scheme of the impact parameter variable. Image taken from [20]



Chapter 4

CMS Detector

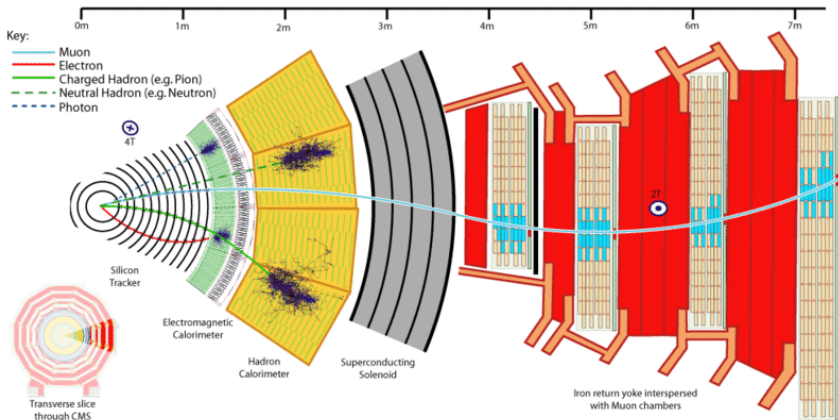
In this analysis we are going to perform simulations of collisions occurring at the CMS experiment, so we have to take into account the specific characteristics of this detector. For this reason, the components of the CMS detector are going to be explained. The CMS detector is one of the seven experiments located at the Large Hadron Collider (LHC), which is the largest and most powerful particle accelerator in the world. This accelerator collides protons and heavy ions at very high energies of the order of 13 TeV and 6.37 TeV, respectively, with the objective of studying the elementary particles that compose the universe.

The LHC is conformed by a ring of almost 27 km of perimeter and by 7 detectors located at the different collision points of the ring. ATLAS and CMS are general purpose experiments and are the largest detectors at the LHC. Both experiments share the same goals of searching physics beyond the SM. The physics program of these experiments includes measurements of the Higgs boson, Supersymmetry searches, dark matter, detection of extra dimensions, among others. The difference between both experiments is that they use different detector designs and software. In the ATLAS detector, the magnetic field is produced by a central toroid, two end toroids, and a central solenoid, while the CMS detector is built around a superconducting solenoid magnet.

The CMS and ATLAS detectors have a cylindrical form in order to have the most uniform magnetic field possible. They are centered in the direction of the interacting beams and the collision point and have two

“end-caps” to cover the forward regions. These detectors are conformed by the same general components, from the inner part of the detector to the outer part. These components are: a tracking system, an electromagnetic and a hadronic calorimeter, and muon detectors. They also have magnets to curve the path of particles with electric charge, so it can be determined whether a particle has a positive or negative charge. Additionally, the measurement of the curve can be used to calculate the momentum of the charged particle. In Figure 4.1, there is a diagram showing the structure of the CMS detector. This image also shows the interaction of different particles with the parts of the detector.

Figure 4.1: CMS detector. Image take from [21]



4.1 Tracking System

Since every 25 ns there is a collision at the center of the CMS detector and almost 1000 particles are going to be produced, it is necessary to have a tracking system able to record measurements of all the particles that are produced. This tracking system must be located the nearest possible to the region where the collision occurs. The tracking system is used to measure the momentum and vertices of the particles with a high precision. The inner detectors are built with silicon detectors, with high granularity pixel

systems at the smallest radii, and silicon-strip detectors at larger ones [22].

The properties of the tracking system are: fast recording of measurements, tolerance to high radiation doses, ensembled with light material and tolerance of the severe conditions imposed by the low temperature at LHC (of almost 2 K). One of the major challenges for the inner detector parts is the control of aging effects because the damage produced by irradiation is severe. The silicon detectors are p-n junction diodes, so when a particle crosses the detector, it causes the liberation of electron-hole pairs, which move to the electrodes of the system. The tracking system in the CMS detector covers the range within $|\eta| < 2.5$, the region where most of the relevant particles for the analysis arrive.

The flux of particles arriving to a point in the detector depends on the distance from the center of collision to where the detector is located: as the flux crosses the detector material the quantity of particles decreases. Thus, the resolution of the tracking system does not need to be so high in the intermediate and end caps regions. For this reason, in the first region of the tracking system (the closest to the interaction point), there are silicon pixel detectors with cell size of $100 \times 150 \mu\text{m}^2$. The innermost layer of pixels is located as near to the beam as it is practical, this is at a radius around 4.5 cm.

The silicon pixels are expensive and have high power density. Additionally, the flux of particles at an intermediate region of the inner detectors is low enough to use silicon microstrips. Thus, in the region of radius greater than 20-55 cm, the silicon pixels are replaced by silicon microstrips. These silicon microstrip are arranged in a special way to improve the resolution in the z axis. These barrel cylinders and end-caps disks, as the silicon pixels, cover the region of $|\eta| < 2.5$. The strip dimensions are around $11\text{cm} \times 100\mu\text{m}$.

In the outermost region of the tracking system (at a radius greater than 55 cm) the particle flux is low enough to use larger-pitch silicon microstrips. The maximum size of these cells is $25\text{cm} \times 80\mu\text{m}$. There are 6 layers of these silicon microstrips modules in the barrel and 9 end-caps disks that also cover the region given by $|\eta| < 2.5$.

4.2 Calorimetry

Surrounding the tracking system of the CMS detector are located the electromagnetic and hadronic calorimeters. The calorimeters measure the energy of the incoming particles by absorbing the particles and transforming them into heat. The priorities of the electromagnetic calorimeter are to measure precisely the energy of electrons and photons, and to make measurements of their position and direction of movement. The priorities of the hadronic calorimeter are to make precise measurements of the jets energy and to cover a larger area of $|\eta| < 5$. The area covered has to be large with the purpose of attributing all the \vec{E}_T^{miss} to the particles that cannot be detected [22].

The electromagnetic and hadron calorimeters are made out of scintillation crystals. When a high energy particle goes through the detector, it collides with the nuclei of the material and generates a shower of particles. The product particles of this interaction excite the atoms in the material by making the electrons in the material go to a higher orbit. When each electron returns to the initial orbit, it emits a photon.

Then, the light emitted by the scintillator is measured by photodiodes, which have the function of converting the optical signals into electronic signals. The photodiodes mechanism is based on the photoelectric effect: the photons emitted by the scintillator arrive to the light-sensitive area of the photodiode and expulse electrons in this surface. Then, these electrons are accelerated and strike a silicon diode target, which causes that more electrons get expelled of this surface. At the end, one obtains an amplification of the initial signal which is measured.

4.2.1 Electromagnetic Calorimeter

The electromagnetic calorimeter is an entirely active homogeneous calorimeter made of lead tungstate (PbWO_4) crystal. It has 61,200 crystal in the central barrel part and 7,324 in each of the two end-caps. As a consequence from the use of high density crystals, the calorimeter is fast, has fine granularity and is radiation resistant.

The lead tungstate crystal material was chosen for different reasons. First, it emits a short radiation length which is easy to record. Second,

it has small Moliere radius, which is defined as the radius of the cylinder surrounding the 90% of the shower's energy deposition. That leads to a compact calorimeter in size. Third, the lead tungstate crystal has short decay time constant, which allows the calorimeter to have a fast response. Lastly, it is resistant to high doses of radiation. Moreover, due to the electromagnetic calorimeter is located within the solenoid, avalanche photodiodes are used as photodetector because they can operate under the magnetic field of 4T [22].

4.2.2 Hadron Calorimeter

Surrounding the electromagnetic calorimeter is located the hadron calorimeter. Its objective is to measure the energy and direction of jets. It is designed to detect the most possible particles product of a collision, so it is said that the detector has a hermetic coverage. The priority of this calorimeter is to determine as correct as possible the missing transverse energy ($E_T^{\vec{miss}}$). The hadron calorimeter is made out of plastic scintillator tiles with wavelength-shifting fiber. The wavelength-shifting is used to shift the wavelength of the light emitted by the scintillator in a the range in which the efficiency of the photodiodes is high [22].

The hadron calorimeter is restricted to fill the area between the outer cap of the electronic calorimeter and the magnet coil, this is $1.77 \text{ m} < R < 2.95 \text{ m}$. The layers of the scintillator tiles are alternately placed with layers of copper in the barrel to form the hadron calorimeter. The end-caps of the calorimeter covers the area of pseudorapidity given by $|\eta| = 3$ and $|\eta| = 5$.

4.3 Muon Detector

The muon system detector consists of several multi-layer large area gas-based detectors. The main objective of this detector is to take precise measurements of muon tracks. Since the muon system detector is located at the outermost part of the CMS, the radiation level it receives is very low in comparison to the tracking system and the calorimeters. The CMS muon detector has three tasks: to identify the muon particles, measure its momentum and triggering on them (this concept is explained in the next

subchapter). The layers of the muon detector alternate with layers of the yoke where the magnetic field returns, which is called flux-return yoke [22].

The flux-return yoke curves the path of the particles in the opposite direction as it was inside the copper layers. It also can be used for good resolution muon identification because it absorbs some hadrons with low energy. The high magnetic field applied and the flux-return yoke allows to take precise measurements of the muon momentum. The muon system detector surrounds the hadron calorimeter and consists also of a barrel section and two end-caps.

The CMS detector has three types of gaseous particle detectors for muon measurements. In the barrel region where the neutron-induced background is low and the magnetic field is almost uniform, there are located drift chambers. The drift chambers are tubes each of 4 cm wide that contain a stretched wire immersed in a gas. When a muon crosses the chamber, it hits the electrons of the atoms in the gas. Then, the free electrons arrive to the positive charged wire and an electronic signal is measured. By measuring the time it takes for an electron to arrive to the cathode (known as drift-time) and the velocity of the free electrons (drift velocity), it is possible to determine the position of the initial muon [23, 14]. The drift chambers cover the region of pseudorapidity given by $\eta < 1.2$.

In the two-end caps regions there are cathode strip chambers (CSC). In these regions the muon rates and backgrounds levels are high and the magnetic field is large and non-uniform. The CSC uses the same principle as the drift chamber to measure the position of muons. The difference is that the CSC consist of anode wires crossed with cathode strips, and these arrays are also immersed in a gas. When a charge particle crosses the detector, it hits the atoms of the gas expelling electrons. The free electrons are guided by the electric field and arrive to the anode wires, while the positive ions move towards the cathode [24]. The CSC have fast response time, fine segmentation and are radiation resistant. Thus, they are able to take precise measurements of time and position. These detectors cover the area given by $|\eta| < 2.4$. Due to the fact that the tracking system and muon detectors take independent measurements of the muon momentum, it is possible to find errors and check both measurements [22].

An additional redundancy in the muon measurements is contributed by resistive plate chambers (RPC) in the barrel and the two end-caps regions.

It is similar to the other two muons detectors: it is conformed by two plates, one is the cathode and the other the anode and these plates are separated by a gas. When a charged particle crosses the detector, the resulting free electrons move to the anode. The electric signal is received by metallic strips after a precise time delay [25]. The set of hit strips gives a precise measurement of the muon position and momentum.

4.4 Triggers

Since at the LHC there are bunch crossings every by 25 ns with a peak crossing rate of 31.6 MHz, nearly a billion proton-proton events are produced every second. Thus, it is necessary to decide if an event must be stored or not in order to use the computational resources in an optimal way. Triggers have the task of applying a primary selection on the data at real-time. The triggers take the data and quickly decide which events that are interesting pass to the next phase of filtering. The triggers need to have a rejection factor of almost 10^7 . As a consequence, it allows to store just around 100-200 carefully selected events per second to be processed later.

The first triggering level uses a partial amount of the total information given by the detector and makes decisions in less that 3.2 ns. It reduces the data rate to nearly 100 kHz [26]. High level triggers use a network of thousands of processors and fast switches. They get the information gradually and use algorithms in order to reduce the amount of data. The final product is that at a rate of 150-200 Hz each event occupies around 1.5 Mb. Under these circumstances, the volume of data processed at the LHC every year is of the order of 10 PB [22]. After an event passes the first triggering level, the resulting data is transferred from the detector electronics into readout buffers. Then, the signal is processed and compressed while the events are studied by processors with several thousands of central processing units. The event then is directed to a single processor with the objective of performing detailed calculations of the critical parameters and reduce the amount of data.

Chapter 5

Modeling of signal and backgrounds

5.1 Signal of Interest

The model that was studied is based on a recently proposed new mechanism of production of heavy neutrinos through the Higgs Boson decay [8]. One favourable characteristic of this model is that, in a natural scenario, the mass of the heavy neutrinos can lie at the electroweak scale. The theoretical study of [8] proposes the experimental search of the heavy neutrinos using a technique known as displaced vertices.

According to this model, when the mass of the heavy neutrinos is inferior than the mass of the Higgs, the latter can present novel decay channels. The Higgs boson can decay into a light and a heavy neutrino, followed by a subsequent decay of the heavy neutrino via a charged or neutral current interaction. Then, the decays of the heavy neutrino can be represented by: $N \rightarrow l^+ l^- \nu$ or $N \rightarrow l q q'$.

If the heavy neutrino has a mass of the order of a few GeV, the Higgs and heavy neutrino would travel a certain distance before decaying. Since both particles are not detected directly, the decay products are expected to have associated tracks with displaced vertices. For this reason, the presence of displaced vertices in the detector is an important signal to prove this model because it could indicate the presence of the heavy neutrino in the detector.

Nevertheless, in this model the resulting leptons have a low momentum. Thus, due to experimental restrictions of the available triggers in CMS and ATLAS, the theoretical analysis proposed in reference [8] is not achievable.

The High Energy Physics Group at Universidad de los Andes has proposed a technique that allows to study at the LHC the production of heavy neutrinos through the decay of the Higgs boson. While in the model proposed in [8] considers the production of the Higgs boson through the fusion of two gluons, we consider the Higgs production through the fusion of two vector bosons. These vector bosons (W^\pm, Z^0, γ) come from an interaction process between two quarks. Both quarks belong to protons from opposite beams that will collide in a particle accelerator. The former described process is known as Vector Boson Fusion (VBF) [27].

As a result of the fusion of the two vector bosons, a Higgs boson is produced and the initial quarks that interacted manifest themselves as jets with high transverse momentum in opposite hemispheres of the detector. For this reason, in Experimental Particle Collider Physics, the events in which two jets of high transverse momentum are detected in opposite hemispheres of the detector and with a high separation of pseudorapidity are labeled as candidates for processes of VBF.

There are two possible final states of the event of interest: two leptons, two jets (from the VBF process) and $E_T^{\vec{miss}}$ (due to the neutrino) or four jets (two of the VBF process and two from the quarks of the heavy neutrino decays), $E_T^{\vec{miss}}$ and one lepton. The first type of final state is going to be called leptonic signal, while the second will be referred to as hadronic signal. The Feynman diagrams illustrating the processes already described are shown in Figure 5.1, where 5.1a is the hadronic signal and 5.1b illustrates the leptonic signal.

The two different final states of the signal are determined by the decay of the W boson that is produced from the heavy neutrino decay. The W boson decays hadronically 64% of the time, while the remaining 36% decays leptonically. [16]. Since it is expected that the hadronic signal have a larger branching fraction than the leptonic signal, in this analysis we simulated only the hadronic signal.

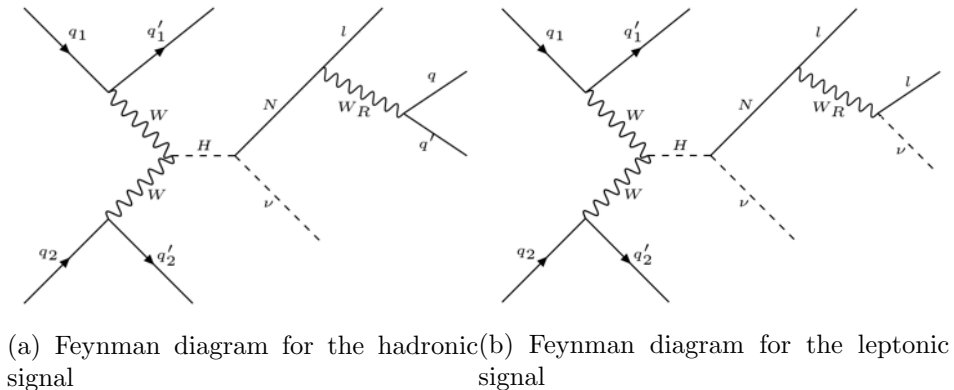


Figure 5.1: Signal Feynman diagrams

5.2 Backgrounds

The main problem of detecting an event of interest is that the magnitude of its signal is significantly smaller with respect to some other processes from the SM. For this reason, the processes from the SM that have the same or similar final states as the signal are called backgrounds.

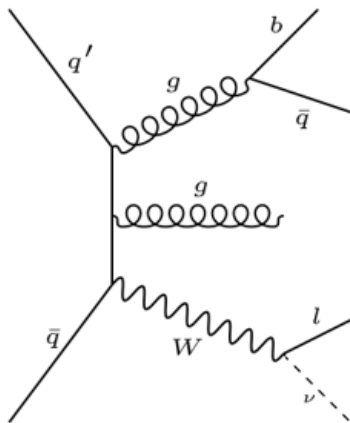
In this analysis, it is fundamental to develop procedures in order to reduce the number of events of background. These procedures usually use different variables (like the ones explained in the chapter 3) that exploit the topology of the event and its kinematic characteristics. When a set of variables that separate the signal from the background is found, it is necessary to find the optimal values of these variables that allow to reduce as much as possible the background.

The signal of interest that was described had two possible final states. For the hadronic signal: two leptons, two jets and $E_T^{\vec{miss}}$ and for the leptonic signal: four jets, $E_T^{\vec{miss}}$, and one lepton. Thus, the main backgrounds of the signal that have a similar final state are the W+jets background and the DY+jets background. In a inferior magnitude there is other background that comes from the production of quark top pairs, referred to as $t\bar{t}$.

5.2.1 W+Jets Background

Events in which a W boson is produced with associated jets, from initial state radiation processes, has a large probability to occur in the proton-proton collisions at the LHC. In leptonic decays, the W boson desintegrates into a lepton and a neutrino. Sometimes, in these events the particles coming from the interaction of the initial hadrons can produce a spontaneous radiative emission, which then is detected as a jet. It is said that this kind of jet comes from an Initial State Radiation (ISR) process. Thus, when the W boson decays leptonically, the final state is conformed by a lepton, $E_T^{\vec{miss}}$ (coming from the neutrino) and jets from ISR. The Feynman diagram is shown in Figure 5.2.

Figure 5.2: Feynman diagram for the W+jets Background

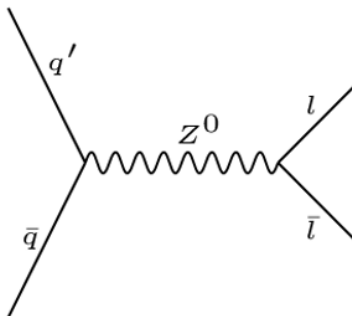


5.2.2 Drell Yan + Jets Background

Other background for our signal of interest comes from the Drell Yan processes. In this process a quark and an antiquark coming from the initial interacting hadrons annihilate each other and this produces a virtual photon or a Z boson. The concept of virtual photon means that this particle is created for a very short period of time. We studied this process only when the Z boson decays into a pair lepton-antilepton, because in this case

the final state is the most similar to the signal. This process was simulated including the production of ISR jets as well. Figure 5.3 shows the Feynman diagram for this process, without including jets from ISR.

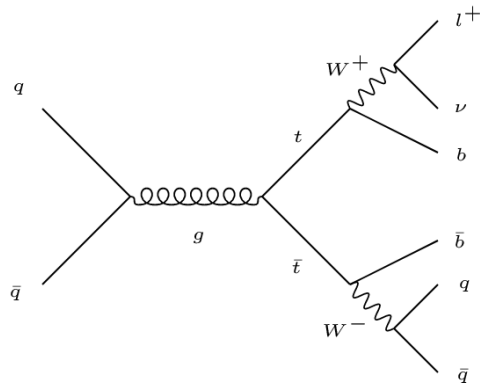
Figure 5.3: Feynman diagram for the DY+jets Background



5.2.3 $t\bar{t}$ Background

Other background for our signal of interest is the production of a top-anti-top quark pair. These events are produced when a gluon coming from the interaction of two colliding protons decays into a pair top-antitop particles. A Feynman diagram for this background is showed in Figure 5.4. This figure shows that the final state of this event has three leptons, E_T^{miss} (coming from the neutrino) and one characteristic jet associated to the hadronization of a b quark. Since the signal does not have the presence of a quark b, this background can be strongly reduced by making the filter of number of bjets equal to zero.

Figure 5.4: Feynman diagram for $t\bar{t}$ Background



Chapter 6

Methodology

The main objective of this project is to perform a feasibility study on the possible identification of heavy neutrinos at the LHC, produced through a Higgs boson decay, using the VBF topology. For this reason, the proposed methodology consists in the use of different computational programs to simulate the signal and the main backgrounds, considering the LHC conditions and detector effects. Next, this data must go through a statistical analysis. The programs that were used to simulate the signal were MadGraph and Pythia. Then, the program Delphes was used to simulate the behavior of the multi-purpose CMS detector. Lastly, the statistical study of the data was developed with the software ROOT, which determined the potential variables that could differentiate the signal and background. In the next paragraphs each program is going to be described, including the fundamental physical basis on which the program is constructed and its specific task in the development of the project.

6.1 MadGraph

The first program that was used is MadGraph, which is a generator of events that simulates the collisions of particle beams, which in our case are protons. MadGraph is written in Python programming language. The physical processes that MadGraph can simulate include processes from the SM and from physics beyond the SM that are based on certain theoret-

ical models such as Supersymmetry. This program incorporates diverse physical parameters in order to include all the necessary elements to make phenomenological studies: it calculates the cross section of a certain event, it generates events with strong interactions (including possible decay of particles) and it offers relevant tools to specify simulation parameters of the events [28].

MadGraph uses perturbation theory to perform cross section calculations and to generate physical processes. The parameter entries are controlled in configuration files that are called input cards. These cards are used to modify essential variables in the production of the events, for example: the type of particles that will collide, the energy of the collision, number of events that are going to be simulated, mass of the generated particles, final states, among others. At the level of event generation, it is possible to make basic cuts of minimal and maximal values of some kinematic variables. Moreover, the latest version of MadGraph (MadGraph 5) has a useful characteristic: it can give an output file with matrix elements that can be used directly in the program Pythia.

In order to produce a process beyond the SM one has to describe the physical model in the form of a Lagrangian, a list of fields, and parameters. Then, use the former elements as parameters input of the MATHEMATICA-based package FEYNRULES. Finally, FEYNRULES returns the Feynman rules corresponding to the Lagrangian of the model, which are used as input of MadGraph [29].

6.2 Pythia

The second computational program that was used is called Pythia. This program receives as parameter input the file generated by the software MadGraph. Pythia incorporates a set of physical models to develop the evolution of a few-body system into a complex multi-particle final state. Thus, the task of the Pythia in the project was to simulate the processes of hadronization of quarks and gluons [30].

6.3 Delphes

This software makes a realistic simulation of the interaction of the simulated particles produced with MadGraph and Pythia with a generic particle detector. The program has ATLAS and CMS cards that can be used to emulate the performance of either detector. The simulation includes a system of track reconstruction immersed in a magnetic field, an electromagnetic calorimeter, a hadronic calorimeter and a muon detection system.

Delphes takes into account the systematic errors that can be generated by the detector, which can be caused by multiple factors such as the resolution of the detectors. This program contemplates different characteristics of the event in the experiment: detector geometry, the track of the charged particles in the magnetic field, reconstruction of the events, and efficiencies of the reconstruction and particle identification [31].

6.4 ROOT

The analysis of the simulated data was performed using the software ROOT. This software was created by the CERN laboratory. ROOT is written in the programming language C++ and it was designed to analyze data in particle physics. This program provides all the necessary tools to efficiently process large amounts of data, make statistical analyses, and have graphical interfaces to display the information and functionally to store the data. The program includes a numerous quantity of mathematical and statistical functions, numeric algorithms and methods for analysis of data regression. One key tool ROOT has are the histograms that can even use multidimensional data and estimate their density. The histograms can be manipulated, offer statistical information, and can perform data regressions [32].

The program ROOT receives as input parameter complementary information that allows it to do the best analysis of the signal: characteristics of the detector or configuration settings that were made in the simulations. ROOT includes other components like a command interpreter that makes quicker the analysis process and a graphic interface which contains a flexible set of tools. The former means that the set of tools can be modified using GUI Builder (the graphic interface constructor). This software can be used to analyse real or simulated data that have the same structure and

consists of many events.

Chapter 7

Event Selection Criteria

The analysis of the simulated data started by imposing a minimum value of 20.0 GeV on p_T for b-jets and taus, and of 30.0 GeV on jets that are not associated to taus or b quarks. The minimum values required on p_T are imposed in order to preselect the interesting particles. After this was done, it was required a minimum separation distance between taus and muons, taus and electrons, and taus and jets. This is done in order to have well identified and well isolated objects in the event selection. To do this, one has to impose a minimal value on a variable called ΔR , which is defined in Equation 7.1. A $\Delta R > 0.3$ was required between the different particle candidates mentioned above.

$$\Delta R \equiv \sqrt{\Delta\eta^2 + \Delta\phi^2} \quad (7.1)$$

Since it was considered that the event of interest was produced through VBF, in the analysis was necessary to find in each event a jet-pair with the distinctive characteristics of a VBF process in their topology. The jets were required to have $p_T > 50$ GeV, because VBF jets are expected to have large transverse momentum. In addition, the jets must have a large separation gap in η , so a cut of $|\eta| > 5.0$ was imposed. The jets also should be located in opposite hemispheres of the detector. If more than two jets with these characteristics were found in the event, the jet-pair combination with the largest mass was selected. The minimal value of this mass was required to be 100 GeV. In the text that follows, the jet with the highest

momentum is referred to as the leading jet, and the other is known as the subleading jet.

After the preselection process is made, we have to find the optimal values of the variables that allow to reduce the background to its minimum. The required values are known as cuts. The first cut imposed in the analysis was on the number of jets. It was required a maximum number of 5 jets because the signal is expected to have 4 jets. An additional jet is included in order to find the best two VBF jets. The second cut imposed was the presence of just one tau, due to the fact that this is a characteristic expected for the hadronic signal.

Next, the third cut imposed was requiring the number of b-jets to be zero. This cut is applied in order to reduce drastically the contribution from $t\bar{t}$ events. Next, a cut on $E_T^{\vec{miss}} > 20$ GeV was applied, which helps to drastically reduce contamination from strong processes, referred to as QCD. Then, a cut on the absolute value of η of the tau of maximum 2.1 was performed. This value was chosen because the tracking detector covers the range of $|\eta| < 2.5$. Since the isolation cones of the taus have a radius of around 0.4, one has to impose a maximum value on $|\eta|$ of maximum $2.5 - 0.4 = 2.1$.

After the cut on $\vec{E}_T^{\vec{miss}}$ was imposed, the cuts motivated by the VBF process were performed. The first cut guarantees that there are minimum two jets that satisfy the condition on p_T to be candidates of VBF jets. Next, it was required that the product of eta between both jets is negative. This implies that both jets are located in opposite hemispheres, in the endcaps system of the detector. Next, it was imposed a minimum separation in η for both jets, referred to as $\Delta\eta$. The minimal value on $\Delta\eta$ was required to be 3.8, since the VBF jets should have a large difference in pseudorapidity.

Finally, a cut in the sum of the invariant mass of the VBF jets, known as dijet mass, was made. It was imposed a value of minimum 500.0 GeV on the dijet mass, due to the fact that the VBF jets have a large momentum, and this is proportional to the mass.

Table 7.1 shows the preselection values imposed that were mentioned on the initial paragraphs of this chapter. Additionally, Table 7.2 shows all the cuts that were performed in the data with the objective of reducing as much as possible the background.

Table 7.1: Preselection criteria

Variables	Value
$p_T(b-jets) \ \& \ p_T(\tau)$	$>20.0 \text{ GeV}$
$p_T(jets)$	$>30.0 \text{ GeV}$
$\Delta R(\tau, e), \Delta R(\tau, \mu) \ \& \ \Delta R(\tau, jets)$	>0.3
$P_T(VBF_jet)$	$>50.0 \text{ GeV}$
$ \eta(VBF_jet) $	>5.0
di-Jet Mass	$>100.0 \text{ GeV}$

Table 7.2: Cuts on different variables

Variables	Values
$n(jets)$	<5
$n(\tau)$	$= 1$
$n(b-jets)$	$= 0$
$ \eta(\tau) $	<2.1
E_T^{miss}	$>20.0 \text{ GeV}$
$n(p_T(jet) > 50.0)$	≥ 2
$\eta(jet_l)\eta(jet_s)$	<0
$\Delta\eta$	>3.8
di-Jet Mass	$>500 \text{ GeV}$

Chapter 8

Analysis

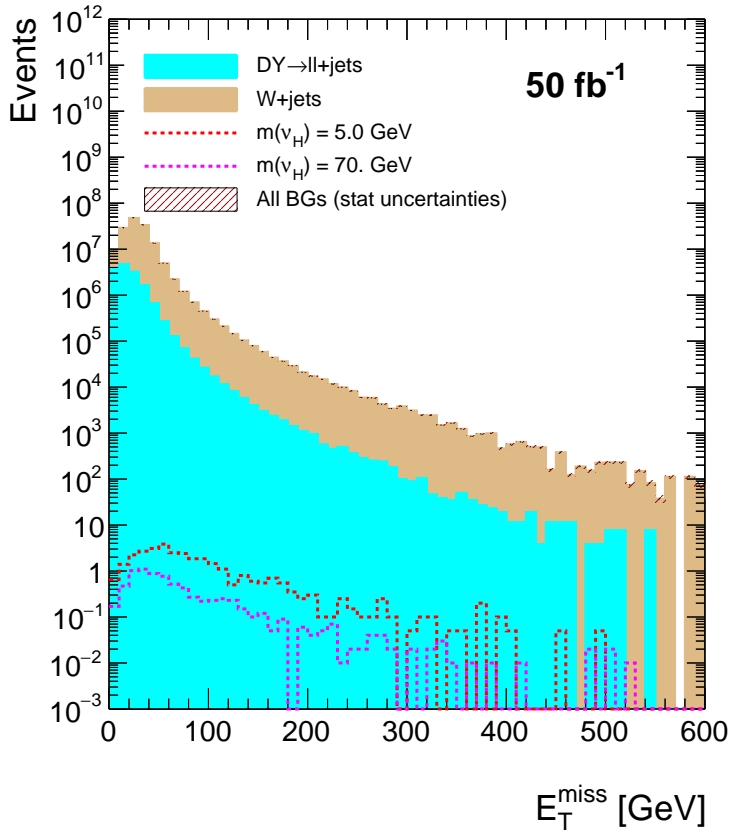
Since MadGraph needs as input parameter the mass of the heavy neutrino, two signals were simulated with different values of mass. One signal was simulated with a neutrino mass of 5.0 GeV, while the other one used a value of 70.0 GeV.

In order to study the performance of a variable to reduce the background, histograms of this variable were made for each signal and background. The type of histograms used in this analysis are called stacked plots. In these histograms each distribution of the variable is placed on the same plot and each one is normalized to the cross section and luminosity. The luminosity expected for the LHC accelerator by the end of 2017 is 50 fb^{-1} . This normalization makes possible to compare the behavior of a given variable for the signal with respect to the given background. In stacked plots the backgrounds are placed sequentially on top of each other, in order to represent a graphical sum of the total noise contribution in the analysis. The signal is drawn overlaid on top of the background. The statistical uncertainty is represented by a dashed line at the top of the background histograms. The plots shown here include just the W+jets and DY+jets backgrounds, because these are very large compared to the $t\bar{t}$ background, and reducing them is already a difficult task.

In the first four plots showed in this chapter some cuts were imposed: the preselection cuts and cuts on the number of jets, taus and b-jets. Figure 8.1 shows the stacked plot of $E_T^{\vec{m}iss}$. It can be seen that the quantity of background events is much larger than the number of events of both

signals at any value of $E_T^{\vec{miss}}$. Moreover, the distribution shape of both backgrounds is alike to the shape of both signals. This implies that a cut on this variable would reduce the background in a similar way as it would reduce the signal. Thus, it is not possible to find an optimal $E_T^{\vec{miss}}$ cut value.

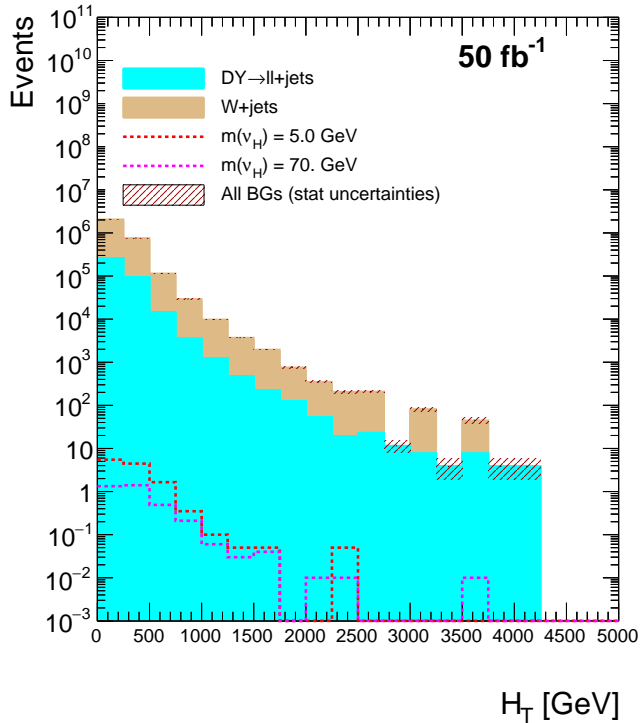
Figure 8.1: Stacked plot of $E_T^{\vec{miss}}$ after the preselection cuts and cuts on the number of jets, taus and b-jets.



We studied the distribution of more variables in order to find possible cut values that can reduce the contribution of background. Figures 8.2, 8.3

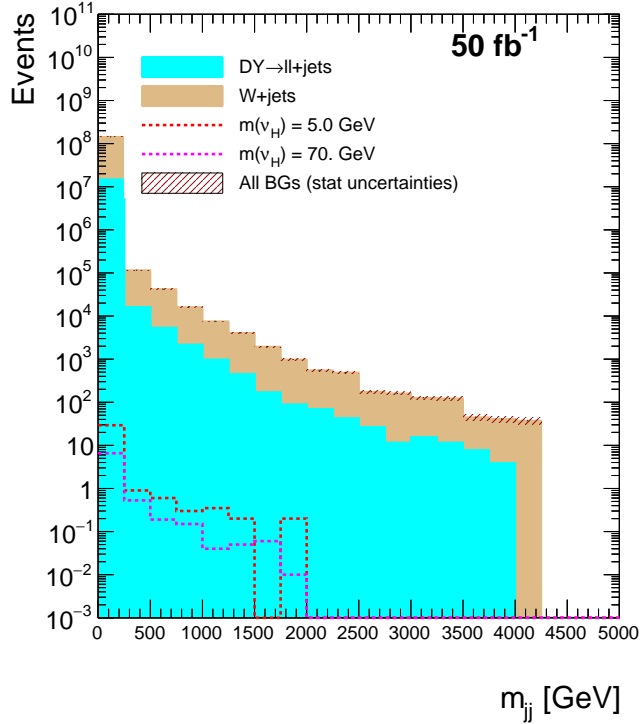
and 8.4 show the stacked plots of the variables H_T , di-jet mass and the tau p_T , respectively. These plots follow an analogous behavior as in the case of $E_T^{\vec{miss}}$: the number of background events is larger than of signal events and the background distribution is similar to the signal distribution. As a consequence, it is not possible to determine a set of variables that allow to reduce the contribution of background.

Figure 8.2: Stacked plot of H_T after the preselection cuts and cuts on the number of jets, taus and b-jets.



Then, all the cuts mentioned in the Chapter 7 are imposed. These cuts include the cuts which take into account the topology of VBF processes. Figures 8.5, 8.6 and 8.7 show the stacked plots of the H_T , di-jet mass and tau p_T variables after all cuts, respectively. It can be seen that the

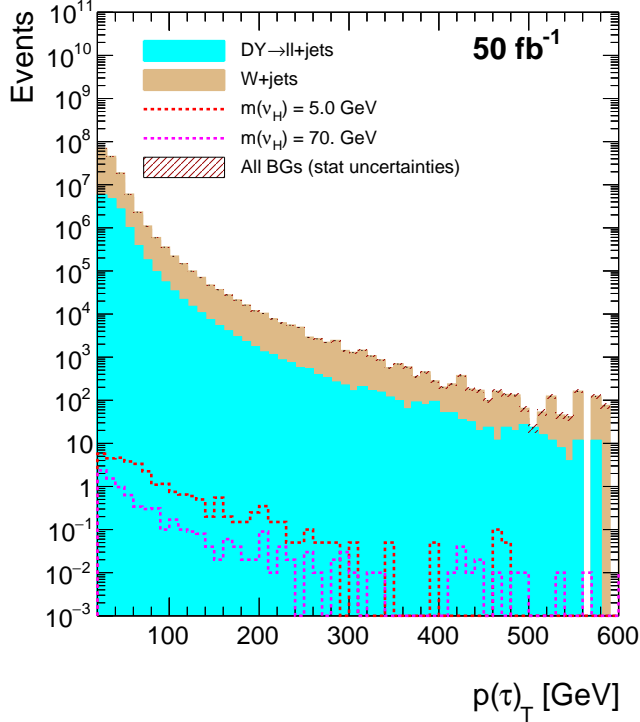
Figure 8.3: Stacked plot of di-jet mass after the preselection cuts and cuts on the number of jets, taus and b-jets.



quantity of background events reduces drastically, but it is still larger than the number of signal events. Moreover, the amount of signal events after imposing all cuts is minimal. Thus, it was not achievable to find a set of cuts that could reduce the background contribution in order to distinguish our signal of interest.

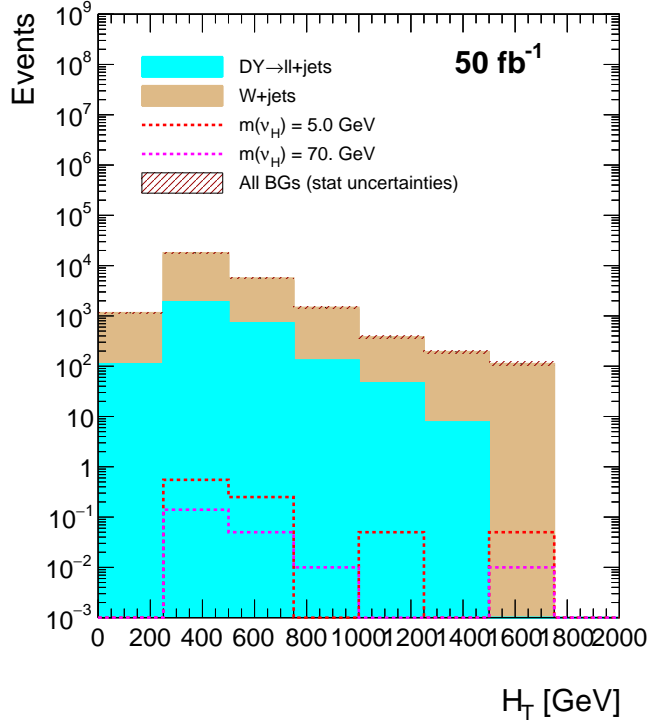
One fact that can explain the reason why VBF cuts do not allow to reduce significantly the number of background events compared to the signal, is that the mass values of the Higgs boson and the Z boson are similar. Since this mass difference is almost just 30 GeV, the production mechanism of a Higgs boson is identical to the Z gamma production mechanism. Thus, the characteristics of the VBF jets in both events are similar and

Figure 8.4: Stacked plot of $p_T(\tau)$ after the preselection cuts and cuts on the number of jets, taus and b-jets.



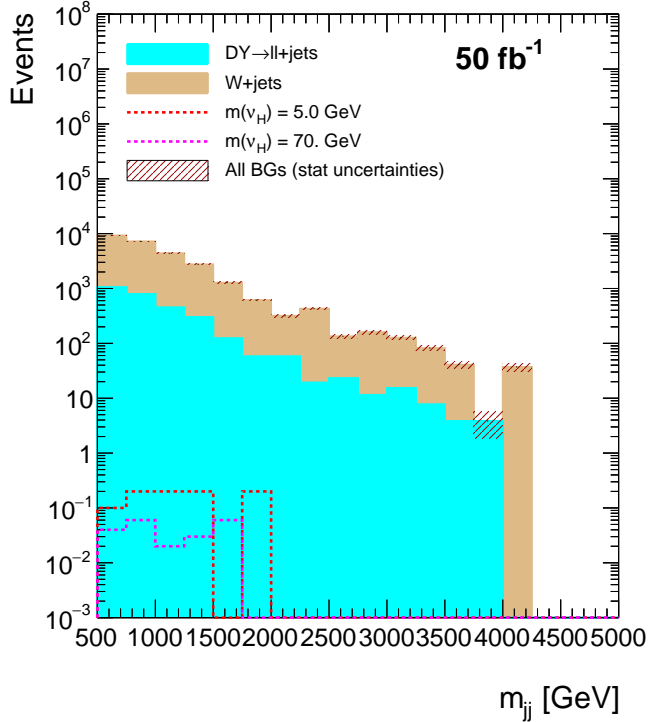
it is difficult to distinguish both VBF topologies. In the case that the heavy neutrinos are produced by the decay of a particle heavier than the Higgs boson, the heavier particle must be the result of an interaction between VBF jets with larger energy. Thus, in this case it would be expected that the detected VBF jets would be more energetic, which could allow to distinguish between both final states.

Since it was expected that the resulting tau in the signal had an associated track with a displaced vertex, some 2D plots were made using this variable. The value of the impact parameter for the tau was found by performing a minimization process on the distance between the tau and the tracks.

Figure 8.5: Stacked plot of H_T after the all the cuts were imposed.

First, we studied a plot on which the x axis represents $E_T^{\vec{miss}}$ and the y axis is the impact parameter (d_{xy}). This plot is shown in Figure 8.8. The first two plots at the left of this figure correspond to the signal events, one assuming a mass of the heavy neutrino of 5.0 GeV, and the other of 70.0 GeV. The range of the y axis for these plots is just from -1.0 to 1.0. The other two plots at the right of the figure correspond to the W+jets background and DY+jets background. These plots have a range in the y axis from -8.0 to 8.0. It can be seen that the impact parameter value of the signals is almost zero. This implies that it is not possible to make a cut on this variable to reduce the background as it was expected. Additionally, it is important to notice that in the case of the signals, the impact parameter

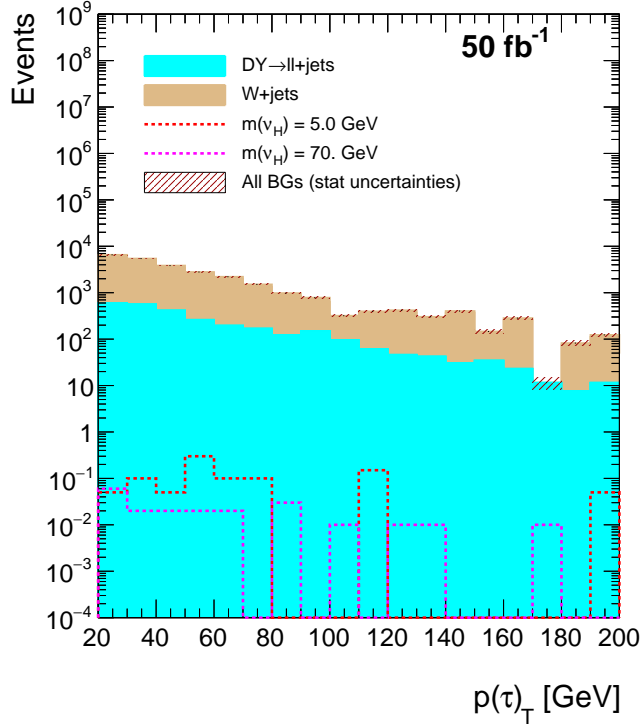
Figure 8.6: Stacked plot of di-jet mass after the all the cuts were imposed.



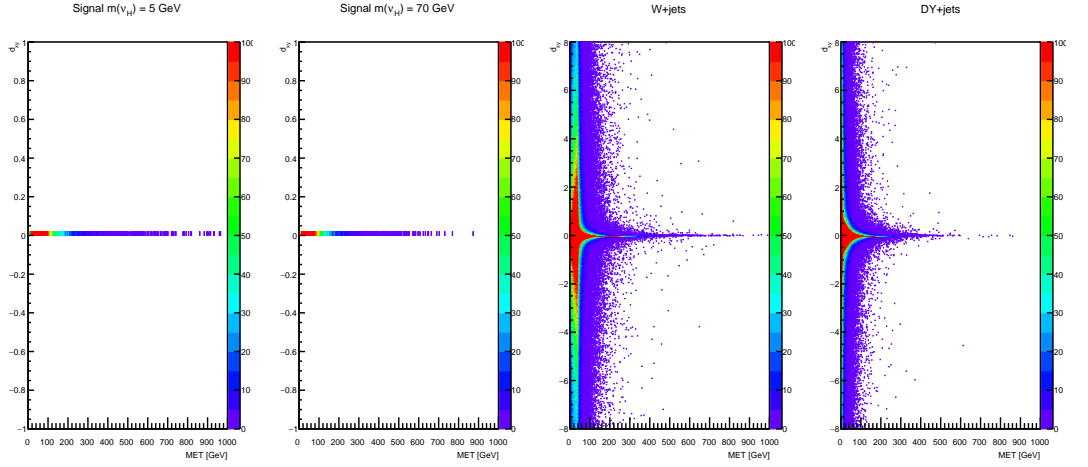
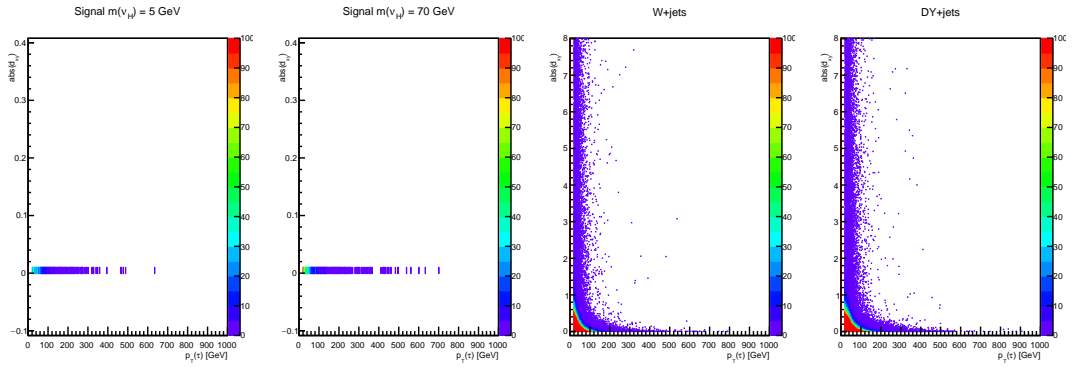
only takes positive values which is not expected since the topology of the events should be symmetrical.

Other 2D plots studied are shown in Figure 8.9. In these plots the x axis represents the tau transverse momentum and the y axis represents the absolute value of the impact parameter. In the signal plots, the y axis has a range between -0.1 to 0.4; while in the background plots it has a range between 0 and 8. Unfortunately, it is not possible to determine a cut value on any of these variables.

Thus, we obtained that the signals of interest present a very low impact parameter value, while it was expected the opposite. Next, possible reasons that can explain the difference between our results and what was expected are discussed. In the first place, the quantity of signal events

Figure 8.7: Stacked plot of $p_T(\tau)$ after the all the cuts were imposed.

simulated is much smaller than the number of background events. Both simulated signals consisted of 10000 events, while the W+jets and DY+jets background samples consisted of millions of events. Thus, we had a small statistical sample and it may be necessary to generate more signal events to make the study. On the other hand, it seemed that there was a problem in the generation of the signals because their impact parameter values were only positive values. The former is not expected because there is no reason to believe that the impact parameter would have an asymmetric distribution. If this problem is solved, a cut on the impact parameter value would significantly reduce the amount of background.

Figure 8.8: 2D plot: E_T^{miss} vs d_{xy} Figure 8.9: 2D plot: $p_T(\tau)$ vs $|d_{xy}|$ 

Chapter 9

Conclusions

The main objective of this work was to perform a phenomenological analysis to determine variables that could reduce the background, to be able to distinguish an event with the presence of a heavy neutrino. In order to do this, we started in Chapter 2 by making a brief summary of the SM and what it states for neutrino mass. Then, we studied the Majorana idea of writing the right-handed field in terms of its left-handed field. The former leads to the description of a Majorana mass term and the definition of a Majorana particle. Then, the Seesaw mechanism and its explanation for the neutrinos mass is discussed. In Chapter 3, the relevant concepts and kinematic variables for this analysis were defined and explained.

In Chapter 4, the different parts of the CMS detector are described with the explanation of how they work and their characteristics. The CMS detector was explained with detail since we considered events produced in this detector. Next, in Chapter 5, it is stated what is expected for the topology of the signals: the presence of a tau with displaced vertex, the presence of high energetic jets related to the VBF process, among other characteristics. The backgrounds of these signals were also explained with their final state characteristics. In Chapter 6, the computational tools that were used in this analysis were described. It was mentioned each software and their specific task on the simulation of the signal and analysis of the data.

Then, the preselection criteria and the different cuts that were applied in this analysis were stated and explained in Chapter 7. Chapter 8 showed

the analysis that was performed to study the signal and its background. It was showed that it was not possible to find optimal cuts in order to reduce the amount of background to distinguish the signal. The former was because the topological distributions of the signal and backgrounds were very similar. This can be caused because the Z boson and the Higgs boson have a similar value of mass. Additionally, the obtained values of the impact parameter for the signals were unexpected, because they all were positive and very small. The former could indicate that there is a problem in the simulation of the signal, since it is expected that the impact parameter has a symmetric distribution.

Appendix A

Neutrinos and Seesaw Mechanism

First of all, we are going to start by defining some fundamental concepts: helicity, chirality and projection operators. The helicity of a particle is defined as the projection of its spin onto the direction of its motion. It is said that a particle is right-handed when its spin is in the same direction as its motion and it is said a particle is left-handed when its spin is in the opposite direction of its motion. In the case of massless particles the concept of chirality and helicity is equivalent. The chirality for a Dirac fermion is defined through the operator γ^5 with eigenvalues ± 1 . Thus a Dirac field can be projected into its left or right component by acting the operators P_R and P_L upon it. The right- and left-handed projection operators are defined as:

$$P_R = \frac{1 + \gamma^5}{2} \quad \text{and} \quad P_L = \frac{1 - \gamma^5}{2} \quad (\text{A.1})$$

A.0.1 Dirac Mass

In this Appendix, we are going to perform with detail the calculations for neutrino physics which were mentioned in the State of the Art Chapter. Now, we start here by studying the Dirac Mass, which is a term of the form:

$$m\bar{\psi}\psi = m(\overline{\psi_L + \psi_R})(\psi_L + \psi_R) = m(\overline{\psi_L}\psi_L + \overline{\psi_L}\psi_R + \overline{\psi_R}\psi_L + \overline{\psi_R}\psi_R) \quad (\text{A.2})$$

Lets study the term $\overline{\psi_L}\psi_L$. Taken into account $P_R P_L = 0$, we obtain:

$$\overline{\psi_L}\psi_L = \overline{\psi}P_L^\dagger P_L\psi = \overline{\psi}P_R P_L\psi = 0 \quad (\text{A.3})$$

Using an analogous reasoning, we can find $\overline{\psi_R}\psi_R = 0$, too. Finally, we got the expression:

$$m\bar{\psi}\psi = m(\overline{\psi_L}\psi_R + \overline{\psi_R}\psi_L) \quad (\text{A.4})$$

A.0.2 Majorana Mass

The expression we had for the Dirac Lagrangian was:

$$\begin{aligned} L &= \overline{\psi} (i\gamma^\mu \partial_\mu - m) \psi \\ &= (\overline{\psi_L} + \overline{\psi_R})(i\gamma^\mu \partial_\mu - m)(\psi_L + \psi_R) \\ &= i\overline{\psi_L}\gamma^\mu \partial_\mu \psi_L + i\overline{\psi_L}\gamma^\mu \partial_\mu \psi_R - m\overline{\psi_L}\psi_L - m\overline{\psi_L}\psi_R \\ &\quad + i\overline{\psi_R}\gamma^\mu \partial_\mu \psi_L + i\overline{\psi_R}\gamma^\mu \partial_\mu \psi_R - m\overline{\psi_R}\psi_L - m\overline{\psi_R}\psi_R \end{aligned} \quad (\text{A.5})$$

We already proved that $\overline{\psi_L}\psi_L = \overline{\psi_R}\psi_R = 0$. Now we are going to study the second term in the Equation A.5, which has a term of the form:

$$\begin{aligned} P_R \gamma^\mu &= \frac{1}{2}(1 + \gamma^5)\gamma^\mu = \frac{1}{2}(\gamma^\mu + \gamma^5\gamma^\mu) \\ &= \frac{1}{2}(\gamma^\mu - \gamma^\mu\gamma^5) && \text{Since } \{\gamma^5, \gamma^\mu\} = \gamma^5\gamma^\mu + \gamma^\mu\gamma^5 = 0 \\ &= \frac{1}{2}\gamma^\mu(1 - \gamma^5) = \gamma^\mu P_L \end{aligned} \quad (\text{A.6})$$

Using what we have found in the last expression, we get for the second

term:

$$\begin{aligned}
i\overline{\psi}_L\gamma^\mu\partial_\mu\psi_R &= i\overline{\psi}P_R\gamma^\mu\partial_\mu P_R\psi \\
&= i\overline{\psi}\gamma^\mu P_L\partial_\mu P_R\psi \\
&= i\overline{\psi}\gamma^\mu\partial_\mu P_L P_R\psi \quad \text{Since } P_L \text{ is a constant operator} \\
&= 0
\end{aligned} \tag{A.7}$$

Following a similar calculation we get: $i\overline{\psi}_R\gamma^\mu\partial_\mu\psi_L = 0$. Our next step is to find the two coupled Dirac equations using the Euler-Lagrange equation. We obtained for the Lagrangian:

$$L = i\overline{\psi}_R\gamma^\mu\partial_\mu\psi_R + i\overline{\psi}_L\gamma^\mu\partial_\mu\psi_L - m\overline{\psi}_R\psi_L - m\psi_L\psi_R \tag{A.8}$$

Replacing in the Euler-Lagrange equation, we get for both states:

$$\begin{aligned}
\frac{\partial L}{\partial(\partial\overline{\psi}_R)} &= \frac{\partial L}{\partial\overline{\psi}_R} \rightarrow 0 = i\gamma^\mu\partial_\mu\psi_L - m\psi_R \\
\frac{\partial L}{\partial(\partial\overline{\psi}_L)} &= \frac{\partial L}{\partial\overline{\psi}_L} \rightarrow 0 = i\gamma^\mu\partial_\mu\psi_R - m\psi_L
\end{aligned} \tag{A.9}$$

Now, we are going to find an expression for ψ_R in terms of ψ_L . First, we take the hermitian conjugate of the bottom equation in A.9:

$$\begin{aligned}
i\gamma^\mu \partial_\mu \psi_R &= m\psi_L \\
(i\gamma^\mu \partial_\mu \psi_R)^\dagger &= m\psi_L^\dagger && \text{Taking the hermitian conjugate} \\
-i\partial_\mu \psi_R^\dagger \gamma^{\mu\dagger} &= m\psi_L^\dagger \\
-i\partial_\mu \psi_R^\dagger \gamma^{\mu\dagger} \gamma^0 &= m\psi_L^\dagger \gamma^0 && \text{Multiplying on the right by } \gamma^0 \\
-i\partial_\mu \psi_R^\dagger \gamma^0 \gamma^\mu &= m\psi_L^\dagger \gamma^0 && \text{Using } \gamma^{\mu\dagger} \gamma^0 = \gamma^0 \gamma^\mu \\
-i\partial_\mu \overline{\psi}_R \gamma^\mu &= m\overline{\psi}_L && \text{We have } \overline{\psi} = \psi^\dagger \gamma^0 \\
-i(\partial_\mu \overline{\psi}_R \gamma^\mu)^\dagger &= m\overline{\psi}_L^\dagger && \text{Taking the transpose} \\
-i\gamma^{\mu\dagger} \partial_\mu \overline{\psi}_R^\dagger &= m\overline{\psi}_L^\dagger \\
-i(-C^{-1} \gamma^\mu C) \partial_\mu \overline{\psi}_R^\dagger &= m\overline{\psi}_L^\dagger && \text{Using } \gamma^{\mu\dagger} = -C^{-1} \gamma^\mu C \\
i\gamma^\mu \partial_\mu C \overline{\psi}_R^\dagger &= mC \overline{\psi}_L^\dagger && \text{Multiplying on the left by } C
\end{aligned} \tag{A.10}$$

As we saw previously, for the last equation to have a similar structure as the top equation of A.9, the right-handed component of ψ must be:

$$\psi_R = C \overline{\psi}_L^\dagger \tag{A.11}$$

Now, we need to prove that $C \overline{\psi}_L^\dagger$ is actually right-handed. To do this we apply the left-handed chiral projection operator P_L on this state and the result must be zero.

$$\begin{aligned}
P_L (C \overline{\psi}_L^\dagger) &= C P_L^\dagger \overline{\psi}_L^\dagger && \text{Property of } C: P_L C = C P_L^\dagger \\
&= C (\overline{\psi}_L P_L)^\dagger
\end{aligned} \tag{A.12}$$

Now, let us examine the term $\overline{\psi}_L P_L$:

$$\begin{aligned}
\overline{\psi}_L P_L &= (P_L \psi)^\dagger \gamma_0 P_L = \psi^\dagger P_L \gamma_0 P_L \\
&= \psi^\dagger \gamma^0 P_R P_L = 0
\end{aligned} \tag{A.13}$$

Hence $C \overline{\psi}_L^\dagger$ is in fact a right-handed chiral state.

A.0.3 Seesaw Mechanism

Now, let us find the neutrino mass eigenvalues by diagonalizing the matrix M :

$$M = \begin{pmatrix} m_L & m_D \\ m_D & m_R \end{pmatrix} \quad (\text{A.14})$$

In order to find the mass eigenvalues we need to solve the equation:

$$|M - I\lambda| = \left| \begin{pmatrix} m_L - \lambda & m_D \\ m_D & m_R - \lambda \end{pmatrix} \right| = 0 \quad (\text{A.15})$$

We obtain a quadratic equation of the form:

$$\lambda^2 - (m_L + m_R)\lambda + (m_L m_R - m_D^2) = 0 \quad (\text{A.16})$$

Using the quadratic equation to find the values of λ , we get:

$$\begin{aligned} m_{1,2} &= \frac{(m_L + m_R) \pm \sqrt{(m_L + m_R)^2 - 4(m_L m_R - m_D^2)}}{2} \\ &= \frac{(m_L + m_R) \pm \sqrt{(m_L - m_R)^2 - 4m_D^2}}{2} \end{aligned} \quad (\text{A.17})$$

Now, setting $m_L = 0$ and assuming $m_R \gg m_D$, we obtain the following mass eigenstates. For the neutrino field ν_1 the mass is given by Equation A.18, and for the neutrino field ν_2 the mass is give by the Equation A.19.

$$m_1 = \frac{m_D^2}{m_R} \quad (\text{A.18})$$

$$m_2 = m_R \left(1 + \frac{m_D^2}{m_R^2} \right) \approx m_R \quad (\text{A.19})$$

Bibliography

- [1] Gonzalez-Garcia, M., Maltoni, M., & Schwetz, T. (2016). Global analyses of neutrino oscillation experiments. *Nuclear Physics B*, 908, 199-217. <http://dx.doi.org/10.1016/j.nuclphysb.2016.02.0331>
- [2] Balantekin, A. & Haxton, W. (2013). Neutrino oscillations. *Progress In Particle And Nuclear Physics*, 71, 150-161. <http://dx.doi.org/10.1016/j.ppnp.2013.03.007>
- [3] Bhupal, P.S., Mohapatra, R.N., and Zhang, Y. (2016). Heavy right-handed neutrino dark matter in left-right models. Retrieved from <https://arxiv.org/abs/1610.05738>
- [4] Bhupal, P.S., Mohapatra, R.N., and Zhang, Y. (2016). Naturally Stable Right-Handed Neutrino Dark Matter. Retrieved from <https://arxiv.org/abs/1608.06266>
- [5] Almeida Jr., F., Coutinho, Y., Martins Simões, J., Vale, M., & Wulck, S. (2001). Dirac and Majorana heavy neutrinos at LEP II. *The European Physical Journal C*, 22(2), 277-281. <http://dx.doi.org/10.1007/s100520100798>
- [6] Gluza, J., Jelinsky, T. (2015). Heavy neutrinos and the $pp \rightarrow l\bar{l}jj$ CMS data. Retrieved from <http://www.sciencedirect.com/science/article/pii/S0370269315005080>
- [7] Aad, G., Abbott, B., Abdallah, J., Abdel Khalek, S., Abidinov, O., & Aben, R. et al. (2015). Search for heavy Majorana neutrinos with the ATLAS detector in pp collisions at $s = 8 \sqrt{s} = 8$ TeV. *Journal Of High Energy Physics*, 2015(7). [http://dx.doi.org/10.1007/jhep07\(2015\)162](http://dx.doi.org/10.1007/jhep07(2015)162)

- [8] Gago, A., Hernández, P., Jones-Peréz, J., Losada, M., Moreno, A. (2015). Probing the Type I Seesaw Mechanism with Displaced Vertices at the LHC. Retrieved from <https://arxiv.org/abs/1505.05880v2>
- [9] Molinaro, E. (2013). Type I Seesaw Mechanism, Lepton Flavour Violation and Higgs Decays. Retrieved from <https://arxiv.org/pdf/1303.5856v1.pdf>
- [10] Chatrchyan, S., Khachatryan, V., Sirunyan, A., Tumasyan, A., Adam, W., & Aguilo, E. et al. (2012). Observation of a new boson at a mass of 125 GeV with the CMS experiment at the LHC. *Physics Letters B*, 716(1), 30-61. <http://dx.doi.org/10.1016/j.physletb.2012.08.021>
- [11] Aad, G., Abajyan, T., Abbott, B., Abdallah, J., Abdel Khalek, S., & Abdelalim, A. et al. (2012). Observation of a new particle in the search for the Standard Model Higgs boson with the ATLAS detector at the LHC. *Physics Letters B*, 716(1), 1-29. <http://dx.doi.org/10.1016/j.physletb.2012.08.020>
- [12] Neutrino Mass and Direct Measurements. (2015) (1st ed.). Retrieved from https://www2.warwick.ac.uk/fac/sci/physics/staff/academic/boyd/stuff/lec_neutrinomass_writeup.pdf
- [13] Kim, C., & Pevsner, A. (1993). *Neutrinos in physics and astrophysics* (1st ed.). Langhorne, PA: Harwood Academic.
- [14] Grupen, C., Shwartz, B., & Spieler, H. (2011). *Particle detectors* (1st ed.). Cambridge: Cambridge University Press.
- [15] Kirschenmann, H. (2017). Sketch of pp-collision and resulting collimated spray of particles, a jet. Retrieved from <https://phys.org/news/2012-07-jets-cms-energy-scale.html>
- [16] HUERTAS, L. (2016). Estudio fenomenológico de búsquedas de nueva física en el LHC, mediante la producción de pares de staus en conjunto con un jet de ISR. (Master of Science). Universidad de los Andes.

- [17] Fruhwirth, R., & Regler, M. (2000). Data Analysis Techniques for High-energy Physics (Cambridge Monographs on Particle Physics, Nuclear Physics, and Cosmology) (1st ed.). Cambridge University Press.
- [18] Schott, M. (2017). Illustration of the ATLAS and CMS coordinate system. Retrieved from <https://inspirehep.net/record/1294662/plots>
- [19] Azuma, Y. SUSY searches with Displaced Vertices (Disappearing Tracks) in ATLAS. Lecture, Berkeley.
- [20] DORNEY, B. (2017). Visualization of the Impact Parameter (IP, red line) of a track (Image courtesy of Jean-Roch Vlimant, of the CMS Collaboration). Retrieved from <http://www.quantumdiaries.org/2011/06/10/to-b-or-not-to-bbar-b-tagging-via-track-counting/>
- [21] Taylor, L. (2011). Detector overview — CMS Experiment. Cms.web.cern.ch. Retrieved 18 May 2017, from <http://cms.web.cern.ch/news/detector-overview>
- [22] Kane, G., & Pierce, A. (2008). Perspectives on LHC physics (1st ed.). Singapore [u.a.]: World Scientific.
- [23] Taylor, L. (2011). Muon Drift Tubes — CMS Experiment. Cms.web.cern.ch. Retrieved 18 May 2017, from <http://cms.web.cern.ch/news/muon-drift-tubes>
- [24] Taylor, L. (2011). Cathode Strip Chambers — CMS Experiment. Cms.web.cern.ch. Retrieved 18 May 2017, from <http://cms.web.cern.ch/news/cathode-strip-chambers>
- [25] Taylor, L. (2011). Resistive Plate Chambers — CMS Experiment. Cms.web.cern.ch. Retrieved 18 May 2017, from <http://cms.web.cern.ch/news/resistive-plate-chambers>
- [26] LHC collisions. (2017). Lhc-machine-outreach.web.cern.ch. Retrieved 17 May 2017, from <https://lhc-machine-outreach.web.cern.ch/lhc-machine-outreach/collisions.htm>

- [27] Dutta, B., Gurrola, A., Johns, W., Kamon, T., Sheldon, P., & Sinha, K. (2013). Vector boson fusion processes as a probe of supersymmetric electroweak sectors at the LHC. *Physical Review D*, 87(3). <http://dx.doi.org/10.1103/physrevd.87.035029>
- [28] Alwall, J., Herquet, M., Maltoni, F., Mattelaer, O., & Stelzer, T. (2011). MadGraph 5: going beyond. *Journal Of High Energy Physics*, 2011(6). [http://dx.doi.org/10.1007/jhep06\(2011\)128](http://dx.doi.org/10.1007/jhep06(2011)128)
- [29] Alwall, J., Frederix, R., Frixione, S., Hirschi, V., Maltoni, F., & Mattelaer, O. et al. (2014). The automated computation of tree-level and next-to-leading order differential cross sections, and their matching to parton shower simulations. *Journal Of High Energy Physics*, 2014(7). [http://dx.doi.org/10.1007/jhep07\(2014\)079](http://dx.doi.org/10.1007/jhep07(2014)079)
- [30] Sjöstrand, T., Ask, S., Christiansen, J., Corke, R., Desai, N., & Ilten, P. et al. (2015). An introduction to PYTHIA 8.2. *Computer Physics Communications*, 191, 159-177. <http://dx.doi.org/10.1016/j.cpc.2015.01.024>
- [31] de Favereau, J., Delaere, C., Demin, P., Giammanco, A., Lemaître, V., Mertens, A., & Selvaggi, M. (2014). DELPHES 3: a modular framework for fast simulation of a generic collider experiment. *Journal Of High Energy Physics*, 2014(2). [http://dx.doi.org/10.1007/jhep02\(2014\)057](http://dx.doi.org/10.1007/jhep02(2014)057)
- [32] Antcheva, I., Ballintijn, M., Bellenot, B., Biskup, M., Brun, R., & Buncic, N. et al. (2009). ROOT — A C++ framework for petabyte data storage, statistical analysis and visualization. *Computer Physics Communications*, 180(12), 2499-2512. <http://dx.doi.org/10.1016/j.cpc.2009.08.005>